A99-31014

AIAA 99–2118

Lattice Boltzmann Simulations of Micro-Jet Controlled Fuel Injector Flow Fields

S. Menon H. Wang and W.-W. Kim
School of Aerospace Engineering
Georgia Institute of Technology
Atlanta, Georgia 30332-0150

35th AIAA/ASME/SAE/ASEE Joint Propulsion Conference and Exhibit
June 20–23, 1999 / Los Angeles, CA

For permission to copy or republish, contact the American Institute of Aeronautics and Astronautics
1801 Alexander Bell Drive, Suite 500, Reston, VA 22191–4344

Lattice Boltzmann Simulations of Micro-Jet Controlled Fuel Injector Flow Fields

S. Menon* H. Wang †and W.-W. Kim‡
School of Aerospace Engineering
Georgia Institute of Technology
Atlanta, Georgia 30332-0150

Next generation combustors must maintain combustion efficiency while considerably reducing emissions, such as, CO, NOx and unburned hydrocarbons. A viable methodology is to enhance the fuel-air mixing process so that the initial dense spray regime is minimized and the subsequent mixing between the vaporized fuel and air is maximized. Current investigations of mixing methods using MEMS-based micro-jet injectors have demonstrated a possible active control method for rapidly increasing the mixing process. However, detailed understanding of the coupling between the MEMS device and the fuel injector is not yet available. In this research, a Lattice Boltzmann equation (LBE) method is employed to simulate the flow both inside and outside a synthetic jet actuator. Effect of varying the forcing amplitude and frequencies, and different configurations of the synthetic actuators are examined. Analysis of these cases, along with comparison with experiments are carried out to demonstrate the accuracy and efficiency of this approach. Subsequently, a fuel injector with synthetic jet actuators inside it is used to demonstrate mixing enhancement by these devices.

1 Introduction

Advances in aircraft gas turbine combustor design are required to satisfy future emission constraints mandated by federal and international requirements. Maintaining combustion efficiency and flame stability while simultaneously reducing NOx (and CO and unburned HC during takeoff/landing) emissions is not feasible without innovative changes in the fuel-air mixing process.

Current attempts are focussed on modifying the fuel-air mixing by changing the pattern of the fuel injected into the combustor. Designs such as multiple injection using micro-laminate screens and advanced swirler cups are currently under study. These concepts are methods that will quickly breakup the initial dense spray regime to develop a relatively well characterized dilute spray pattern so that both the fuel-air mixing and the subsequent combustion process can be controlled as required. The dense spray regime which occurs as the liquid fuel exits from the nozzle (and therefore, plays a major role in the subsequent spray pattern) is a major area of uncertainty since the process of liquid breakup, the formation of ligaments followed by ligament stretching and turbulent distortion, and, finally, breakup, are not understood very well. Thus, it is clear that an approach that will minimize, if not eliminate, the dense spray regime could go a long way towards developing a controlled spray pattern and hence, allow efficient fuel-air mixing.

An underlying feature of the above noted design concepts is the passive approach to mixing enhancement. This has been necessary since these fuel injectors have to operate in a hostile (hot) environment and must deliver the requisite fuel pattern over a wide operating regime. Active control of fuel injection has only recently been explored, but recent results suggest that robust active methods could be built which can extend the operating margin of the fuel injection system. Such an approach has the potential for providing a new means for controlling the combustion process even under conditions that are not allowed to occur in current designs. For example, flame stability in the lean limit, control during high pressure combustion and efficient combustion using new exotic fuels(e.g., supercritical) are all potentially operational scenarios that may be achieved using active control.

As an example of recent innovation, recent experiments have demonstrated the ability of microelectromechanical systems (MEMS) such as micro injectors and synthetic jet actuators[1-3] to control and modify the dynamics of primary jet flow. Experiments have shown that the primary jet spreading

---

*Professor, AIAA Senior Member

†Graduate Research Assistant

‡Post-Doctoral Fellow, AIAA Member

rate can be significantly enhanced by using these micro-injectors along the circumference of the jet nozzle. An obvious practical application is enhancement of fuel-air mixing. Note that these micro injectors may function as expected in real combustors if they are inside the primary fuel injector nozzle and, therefore, relatively protected from the hot environment. So far, the effects of the MEMS devices have been ascertained only indirectly by observing the primary jet flow since detailed quantitative measurements in the vicinity of the micro injectors are difficult, if not impossible. Furthermore, all studies so far have been limited to non-reacting flows and to relatively large devices. For example, recent studies at Georgia Tech employed synthetic jets with exit diameter of 8 mm to control a primary air jet of around 25 mm. However, practical fuel injectors have typical dimension of 1-3 mm which implies that the synthetic jet diameter needs to be around 0.1 mm or smaller. Under these conditions, detailed measurements in the near field are going to be very difficult.

To demonstrate the ability of MEMS devices to control fuel injectors in a practical combustor optimization of these devices (including design, placement and forcing conditions) is required. Although this could be attempted experimentally by carrying out parametric studies, a numerical predictive capability, if available, would go a long way towards providing the necessary data for optimal design. Recently, some numerical studies of the flow field in the vicinity of a synthetic jet have been reported.[4] However, all these studies were limited to non-reacting flows and simulated the synthetic jet in isolation. Thus, the coupling of the synthetic jet with the primary fuel jet has not yet been investigated.

All the above noted numerical studies[4,5] were also carried out using conventional Navier-Stokes codes. Although this approach is acceptable for most conditions of interest, it must be noted that under certain conditions, the scale of the MEMS device (i.e., submicron scale) may be so small and the flow conditions may be such that the continuum assumptions may be questionable.[6] Under these conditions, an alternate methodology is required. Past studies have employed the Navier-Stokes method with velocity-slip and temperature-jump conditions[6] as well as the Direct Simulation Monte Carlo (DSMC) methods.[7,8] DSMC method is optimal for free molecular flows but becomes computationally prohibitive in the continuum regimes due to the large number of particles that must be tracked. On the other hand, velocity-slip condition is valid only in the near-continuum regime($Kn = \lambda/L \doteq 0.1$, where Kn is the Knudsen number, λ is the mean free path and L is the characteristic length scale) and cannot be employed when the local flow conditions do not satisfy continuum assumptions. An alternate methodology that has the potential to study the entire regime from non-continuum to continuum flow is the Lattice Gas Automaton (LGA) Method or its more recent variant, the Lattice Boltzmann Equation (LBE) method[9-11] 1995). Both these methods (which are similar to DSMC method) have been demonstrated in various types of flows including two-phase and reacting flows.[11]

Results have demonstrated that the LBE method is superior to the LGA method and (1) can be used to study flows in complex (3D) configurations (a requirement essential to simulate typical micro injectors of current interest),[10] (2) reproduces the Navier-Stokes equations in the continuum limit (3) is computationally very efficient and inherently parallel, and, (4) is applicable to low Re and low Mach number flows (typical in micro injectors).

This paper discusses the application of LBE method to simulate the flow both inside and outside a synthetic jet and further investigates the mixing efficiency of these synthetic jets when placed inside a fuel injector. Note that, the present study is in the continuum regime and therefore, both LBE and conventional Navier-Stokes methods are equally applicable. However, as shown here, the LBE method is computationally much more efficient (in fact by orders of magnitude) when compared to a typical finite-volume method. Furthermore, another advantage of the LBE method is that it has the potential for application even in the transition regime (near continuum, $0.1 < Kn < 1$) by proper modifications to the collision integral in the Boltzmann equation.

2 Lattice Gas and Boltzmann Methods

The Boltzmann equation is the fundamental equation that governs all fluid motion from free molecular flow to continuum flow. This equation is derived using kinetic theory and is an equation for the probability density function (pdf) for the molecular motion in phase space. The phase space is a 7 dimensional space of the physical space $\mathbf{x}$, the velocity space $\mathbf{v}$ and time t. The pdf of the molecular distribution is defined as $f(\mathbf{x}, \mathbf{v}, t)$ and a partial differential equation for the evolution of the pdf can be derived, as shown in the classical text books.

The Boltzmann equation is valid in all regimes of fluid motion from the free molecular regime ($Kn >> 1$) to the continuum regime ($Kn << 1$) and when integrated over the velocity space, the Boltzmann's equation recovers the well-known continuum Navier-Stokes equations of motion.

The present study exploits the capability of the Boltzmann equation in a numerical model to simulate flow in the continuum regime.

2.1 Lattice Gas Method

LGA method is a particle based (as is DSMC) method and involves particle-particle interactions based on collision rules and conserve locally total mass, momentum and energy exactly, with no round-off error. Therefore, these algorithms are unconditionally stable. In the original LGA method, space and time are discrete, particle representation is based on integer bits, and the motion of individual particles is followed along a pre-specified lattice (or grid). For example, in 2D hexagonal lattice there are six nonzero momentum states associated with the directions to the nearest neighbors. Using an exclusion principle (i.e., only one particle at a given site), the LGA method involves two discrete time steps: particle motion due to their local momentum direction and particle collision when it encounters another particle in the adjacent site. The collision rules are such that local conservation is enforced and since particles are represented using integer bits, update of states in the lattice can be carried out very fast. It has been shown that by taking the ensemble average of the particle states and by assuming molecular chaos, the continuum version of the kinetic equation is obtained from which the fluid equations can be derived by using Chapman-Enskog expansion.[9,12,13]

There are, however, some limitations of the LGA method. This approach results in a non-Galilean advection of the velocity field and a velocity dependent term appears in the pressure. In addition, unless a long time average is employed, the LGA result will contain stochastic noise that is numerical in nature and very difficult to eliminate. Although methods to reduce the noise and to obtain appropriate equation of state have been demonstrated, there remains some uncertainties when using the LGA method for real practical flows.

2.2 Lattice Boltzmann Method

A variant the LGA approach is the Lattice Boltzmann Equation (LBE) method in which, instead of bit representation of particles (as in LGA method), real numbers represent the local ensemble-averaged particle distribution functions and only the kinetic equation for the Boltzmann distribution function is solved (whereas, in LGA methods individual particle motion is explicitly tracked in the lattice). The LBE method can be viewed as a type of finite-difference technique for the solution of the Boltzmann equation. There are some significant advantages of this approach. The LBE method eliminates most of the noise in the LGA method, recovers the Navier-Stokes equation in the low frequency and long wavelength limit, removes the velocity dependence of pressure, and is Galilean invariant (see cited references). In application, this method is purely local, inherently parallel and very fast. An important feature is that (unlike conventional finite-difference methods) LBE method has the same speed and efficiency in both simple and complex geometries.[14] Properly optimized parallel codes have been developed in the past and have demonstrated near teraflop capability (as noted above). Furthermore, these methods can be used for both compressible and incompressible 3D flows,[15,16] and are particularly suited for low Re flows.

In the following, we briefly summarize the LBE model in two-dimensional (2D) flows. Three dimensional models will be addressed in the future.

2.3 Two-dimensional 9-bit LBE model

The LBE method essentially solves the Boltzmann equation in the phase space (physical space, velocity space and time). A recent study[17] showed that the LBE method can also be regarded as a discrete form of the continuous Boltzmann equation, providing that the discretization has a certain order of accuracy.

The key step in the LBE method's implementation is the manner in which the velocity space discretization is carried out. The 9-bit lattice Boltzmann model[9,12] has been shown to be sufficient to recover the Navier-Stokes equations in 2D and is usually used to simulate two-dimensional flows. [Note that for 3D flows, 18 velocity directions are needed to recover the full 3D Navier-Stokes equations]. For more information regarding other LBE models, interested readers are referred to the recent review by.[11]

The 9-bit lattice Boltzmann model simulates fluid flow by tracking the single-particle distribution function at the following nine discrete velocities:

$$\mathbf{e}_\alpha = \begin{cases} \mathbf{0}, \alpha = 0, \\ (\cos[\alpha^*], \sin[\alpha^*])c, \alpha = 1-4, \\ \sqrt{2}(\cos[\alpha''], \sin[\alpha''])c, \alpha = 5-8 \end{cases} \tag{1}$$

where $\alpha^* = (\alpha-1)\pi/2$, $\alpha'' = (\alpha-5)\pi/2 + \pi/4$ and c is a characteristic speed which is related to the sound speed by $c = \sqrt{3}c_s$.

The evolutions of the distribution functions, f_α for $\alpha = 0, 1, , , 8$ is governed by:

$$f_\alpha(\mathbf{x} + \mathbf{e}_\alpha\delta, t+\delta) - f_\alpha(\mathbf{x}, t) = \frac{1}{\tau}[f_\alpha^{eq}(\mathbf{x}, t) - f_\alpha(\mathbf{x}, t)] \tag{2}$$

where τ is the dimensionless relaxation time, e_α is the particle speed in α direction and the characteristic speed is $c = \mathbf{e}_\alpha \delta/\delta = |\mathbf{e}_\alpha|$. Rest particles of type 0 with $e_0 = 0$ are also allowed. Note that the time step and the lattice spacing each have equal spacing of unity. Thus, $\delta = 1$. The equilibrium distribution function, f_α^{eq} is given by the the following form as shown in:[12]

$$f_\alpha^{eq} = w_\alpha \rho [1 + \frac{3(\mathbf{e}_\alpha \cdot \mathbf{u})}{c^2} + \frac{9}{2}\frac{(\mathbf{e}_\alpha \cdot \mathbf{u})^2}{c^4} - \frac{3}{2}\frac{\mathbf{u}^2}{c^2}], \quad (3)$$

where

$$w_\alpha = \begin{cases} \frac{4}{9} & \alpha = 0, \\ \frac{1}{9} & \alpha = 1,2,3,4, \\ \frac{1}{36} & \alpha = 5,6,7,8. \end{cases}$$

Solution of Eq. (2) gives f_α which can then be integrated over the velocity space to obtain the macroscopic variables. For example, the density, ρ, and the velocity field, $\mathbf{u}$, are calculated by

$$\rho = \sum_\alpha f_\alpha, \rho\mathbf{u} = \sum_\alpha \mathbf{e}_\alpha f_\alpha, \quad \alpha = 0, 1, ..., 8. \quad (4)$$

It has been shown that if Chapman-Enskog procedure is applied to Eq.(2), the macroscopic equations of the model (i.e., the Navier-Stokes equations) can be derived subject to an error of $O(\delta^2)$. The N-S mass and momentum equations derived from these equations are:

$$\frac{\partial \rho}{\partial t} + \frac{\partial \rho u_\alpha}{\partial x_\alpha} = 0 \quad (5)$$

$$\frac{\partial(\rho\, u_\alpha)}{\partial t} + \frac{\partial(\rho\, u_\alpha u_\beta)}{\partial x_\beta} = \frac{\partial(c_s^2 \rho)}{\partial x_\alpha} + \frac{\partial(2\nu\rho S_{\alpha\beta})}{\partial x_\beta} \quad (6)$$

Here, repeated indices indicate summation and $S_{\alpha\beta} = \frac{1}{2}(\partial_\alpha u_\beta + \partial_\beta u_\alpha)$ is the strain-rate tensor. The pressure is given by $p = c_s^2 \rho$ where c_s is the speed of sound with $({c_s}^2 = 1/3)$, and $\nu = [(2\tau - 1)/6]$ is the kinematic viscosity. The discussion of the error terms and the derivation of these equations are given elsewhere[13, 15] and therefore, omitted here.

3 Simulation Methodology

The numerical simulation using the LBE method involves three primary steps: collision, streaming and interpolation. These three steps are defined below.

(1) Given an initial particle distribution function at each of the lattice location $\mathbf{x}$, all macroscopic flow properties such as the velocities u, v and pressure p are known everywhere. Also, the equilibrium distribution function f_α^{eq} can be constructed at every lattice point. Then, the first step of collision takes place according to the right-hand-side of Eq. 2. From this step, the post collision value of f_α can be determined; (2) After the collision, advection (also called streaming) takes place and the values of $f_\alpha(\mathbf{x} + \mathbf{e}_\alpha \delta, t + \delta)$ are obtained; (3) The values of $f_\alpha(\mathbf{x}, t + \delta)$ on the mesh grid $\mathbf{x}$ are computed from the values of $f_\alpha(\mathbf{x}+\mathbf{e}_\alpha \delta, t+\delta)$ on the points $\mathbf{x}+\mathbf{e}_\alpha \delta$ by interpolation. This particular step is needed when we employ a non-uniform grid (as done here). Then the collision and the advection steps are repeated.

The model used here has been shown to be second-order accurate in space and time. Accuracy of the scheme is achieved by proper interpolation method when applied on non-uniform grids as well as by using accurate boundary conditions. The implementation of the boundary conditions is especially critical for obtaining correct solution using the LBE method. This issue is discussed below.

3.1 Boundary Conditions

The boundary conditions for the LBE model as applied to the synthetic jet are discussed in this section. Figures 1a 1b show respectively, the velocity directions in the vicinity of a no-slip wall and a concave wall. In Fig. 1a, after streaming, $f_0, f_1, f_3, f_4, f_7, f_8$ are known but f_2, f_6 and f_5 are not known since they depend upon the wall conditions. Suppose that u_x, u_y (the two velocity components) are specified on the wall (obviously they will be zero for no-slip but the following derivation allows for slip wall and blowing/suction conditions). Using Eq.(4), the following relations can be obtained:

$$f_2 + f_5 + f_6 = \rho - (f_0 + f_1 + f_3 + f_4 + f_7 + f_8), \quad (7)$$

$$f_5 - f_6 = \rho u_x - (f_1 - f_3 - f_7 + f_8), \quad (8)$$

$$f_2 + f_5 + f_6 = \rho u_y + (f_4 + f_7 + f_8) \quad (9)$$

Also assuming elastic collision we get:

$$f_2 - f_2^{(eq)} = f_4 - f_4^{(eq)} \quad (10)$$

Equations (7 -10) can be combined to obtain:

$$f_2 = f_4 + \frac{2}{3}\rho u_y, \quad (11)$$

$$f_5 = f_7 - \frac{1}{2}(f_1 - f_3) + \frac{1}{2}\rho u_x + \frac{1}{6}\rho u_y, \quad (12)$$

$$f_6 = f_8 - \frac{1}{2}(f_1 - f_3) - \frac{1}{2}\rho u_x + \frac{1}{6}\rho u_y, \quad (13)$$

The corner nodes (concave and convex corner nodes) need special treatment. For a concave corner node (see Fig. 1b) after streaming, f_3, f_4, f_7

are known, ρ is specified, and $u_x = u_y = 0$ for no-slip boundary condition. We need to determine f_1, f_2, f_5, f_6, f_8. Using elastic collision rules we obtain

$$f_1 = f_3 + (f_1^{eq} - f_3^{eq}) = f_3, f_2 = f_4 + (f_2^{eq} - f_4^{eq}) = f_4 \quad (14)$$

Using f_1, f_2 from the above relation we obtain:

$$f_5 = f_7,\ \ f_6 = f_8 = \frac{1}{2}[\rho_{in} - (f_0 + f_1 + f_2 + f_3 + f_4 + f_5 + f_7)] \quad (15)$$

3.2 Scalar Modeling in the LBE Method

An extension of the LBE method to simulate scalar (temperature or species) is a two-component LBE system.[18] The distribution functions for two components ($i = 1, 2$) evolve according to Eq. (2) and can be expressed as:

$$f_\alpha^{(i)}(\mathbf{x}+\mathbf{e}_\alpha\delta, t+\delta) - f_\alpha^{(i)}(\mathbf{x}, t) = \frac{1}{\tau^{(i)}}[f_\alpha^{(i,eq)}(\mathbf{x}, t) - f_\alpha^{(i)}(\mathbf{x}, t)] \quad (16)$$

In this model, component 1 represents the motion of the fluid and component 2 simulates a passive scalar field. The equilibrium distributions are still defined by Eq. (3) for both the components. Since component 2 is passively advected and diffused into the flow of component 1 without contributing to the total momentum of the mixture, the velocity $\mathbf{u}$ in the equilibrium distribution of component 2 is replaced by the fluid velocity calculated from the distribution function of component 1.

The density and the fluid velocity of component 1 still satisfy the Navier-Stokes conservation equations and the density of component 2 satisfies the conventional diffusion equation of a passive-scalar. The diffusivity of component 2 can be tuned independently of the viscosity by changing the dimensionless relaxation time, τ, of the component 2.

This LBE model can be extended to multi-species and multiphase flows including phase transitions by adding interparticle and inter-component interaction effects, as described elsewhere.[19] We will consider reacting flows in the next phase of this research.

3.3 LBE method on Stretched Grids

The original LBE models were restricted to a uniform lattice in the physical space. Thus, a particle (or an equilibrium distribution) had to move to another lattice site at each time step. This constraint is essential for the "Boolean" calculation in LGA, but becomes redundant in the LBE method, because the particle distribution in LBE models is continuous functions in both space and time. The value of a function at one location in space can be approximately interpolated from the values of the function at the neighboring locations.

Based on the above observation, an interpolation supplemented lattice Boltzmann equation (ISLBE) model has been recently proposed to extend the LBE method to variable grids.[20] Numerical simulations of flow in a sudden expansion[20] and flow around a circular cylinder[21] using the ISLBE model agreed well with benchmark data. A recent theoretical analysis also showed that the ISLBE is at least second-order accurate when a quadratic interpolation scheme is used.

If a flow domain is covered by a curvilinear coordinates system: $\xi = \xi(\mathbf{x}), \eta = \eta(\mathbf{x})$ and the distribution functions are known at all the grid node initially, then, after one time step, according to Eq.(2), the distribution function is known at all the shifted grid nodes, $\mathbf{x} + \mathbf{e}_\alpha\delta$. The coordinates of the original grid nodes in the shifted curvilinear coordinate system can be calculated by interpolation.

4 Results and Discussion

Results demonstrating the accuracy and validity of the LBE method developed here is discussed in this section. Various parameters relevant from design stand point such as the forcing frequency, the forcing amplitude, the jet diameter and the cavity depth were varied systematically to understand the dynamics of the synthetic jet flow field.

4.1 Validation of the LBE code

To validate the 2D LBE model various test cases were studied: flow past a rearward facing step, laminar free jet and turbulent free jet and the results were compared to the experimental data and theoretical results. Earlier studies of flow past a rearward facing step showed very good agreement with experimental data. Here, only the free jet results are discussed since they represent the closest approximation to the synthetic jet case of present interest. The computational domain for these studies is $30h$ both in the streamwise and cross-stream directions, where h is the jet orifice size. The jet enters the computational domain through a slit on the left side of the computational domain. A grid resolution of 221 x 271 is used which is uniform in the jet region and stretched towards the far field. Grid independence studies are discussed later.

The laminar free jet at a Reynolds number 30 (based on the inflow velocity U_0 and the slit height h) and a turbulent jet at a Reynolds number of 9000 are simulated. The jet mean exit velocity profile for both cases were approximated using $U_0[1 - (\frac{y}{h/2})^n]$, where n=2 is used for the laminar jet and n=8 is used for the turbulent jet cases.

Figures 2a and 2b shows respectively, the (normalized) centerline velocity decay as a function of the distance from the jet exit for the laminar and the turbulent jets. The present results agree quite well with the theoretical decay rate of $1/x^{1/3}$ predicted for 2D laminar jet and the decay rate of $1/x^{1/2}$ for the turbulent jet. More detailed comparisons for the turbulent case is not carried out here since the present model is 2D. Note that for the application of interest (i.e., synthetic jet within the fuel injector) the characteristic Reynolds number is expected to be small and hence, the present validation study provides the confidence about the accuracy of the scheme.

4.2 Synthetic Jet Test Conditions

A single isolated synthetic jet was numerically simulated using the LBE method. A key feature of the present approach is that both the region inside the cavity and the flow downstream of the jet exit plane are simulated using the same code. In the actual experiments, the synthetic jet is triggered by vibrating the bottom wall of the cavity (which is made of a piezoelectric material). It is difficult (although not impossible) to mimic this feature in a numerical model. The primary result of the surface actuation is that the fluid adjacent to the oscillating surface is set into motion. Therefore, in the present study, this resulting phenomenon is mimicked by incorporating a blowing/suction boundary condition along the bottom wall of the cavity. This approach therefore, ignores the moving wall effect but provides an appropriate boundary condition to modify the fluid motion inside the cavity (as in the real device). As a result, no explicit control of the the flow exiting from the cavity orifice is needed in this approach. This is in contrast to the approach used earlier[5] where the perturbation to the streamwise velocity component was imposed at the orifice exit itself. This approach imposes a restriction on the flow exiting (and entering) the cavity that is not likely to be realistic.

In the present study, the streamwise velocity perturbation at the bottom wall of the cavity is of the form: $u(t) = U_0 sin\omega t$, where ω is the prescribed frequency and U_o is the forcing amplitude. The effect varying the forcing frequency, the forcing amplitude, the cavity depth and the orifice size was investigated. However, for brevity, we discuss only representative cases. The various cases are summarized in Table 1. The baseline values are $U_o = 20m/s$, $d_o = 1mm$, $h_o = 0.5mm$ and $f_o = 4KHz$.

We used Case 11 (which is similar to an earlier experiment) to carry out validation of the present synthetic jet model. Other cases were used to characterize the behavior of the synthetic jet under various conditions. For a representative parametric comparison, Case 1 was chosen as a baseline case and other cases were compared against this baseline case.

type	forcing amplitude	forcing frequency	orifice size	cavity depth
case1	U_0	f_0	h_0	d_0
case2	U_0	$0.5f_0$	h_0	d_0
case3	U_0	$2f_0$	h_0	d_0
case4	$0.5U_0$	f_0	h_0	d_0
case5	$1.5U_0$	f_0	h_0	d_0
case6	U_0	f_0	$1.5h_0$	d_0
case7	U_0	f_0	$2h_0$	d_0
case8	U_0	f_0	h_0	$0.5d_0$
case9	U_0	f_0	h_0	$2d_0$
case10	U_0	f_0	h_0	$4d_0$
case11	U_0	$0.25f_0$	h_0	d_0

Table 1 Computational Cases for Synthetic Jets

To analyze the results, data was collected after two flow-through times for a period of 4-5 flow-through times (here, a flow-through time is defined as the time it takes for a shed vortex to leave the computational domain). This data was then time-averaged to obtain the stationary state results.

Grid independence analysis was first carried out. The grid was clustered in regions of high shear such as the region near the jet orifice. Furthermore, to ensure that the flow field in the cavity is well resolved, a large number of grid points was used in that region. Grid was also clustered near all the wall regions. To resolve the entire domain, grid needs to be stretched from these regions of high resolution. However, to maintain at least second-order accuracy, the grid stretching was sufficiently small: a stretching factor of 1.005 in the streamwise direction and 1.045 in the cross-stream direction was employed. Due to these restrictions, a typical 'low' resolution grid was of the order of 321 x 325 for the domain of interest which was 10 mm in both the cross-stream and the streamwise directions for a orifice width of 0.5 mm. A typical domain and grid is shown in Fig. 3.

We compare here results obtained using two different grids: 321 x 325 and 375 x 525. The resolution was increased in the cross-stream direction primarily to ensure that the regions of high shear are sufficiently resolved. As shown in Fig. 4 there is no noticeable differences between the results obtained using these two grid resolutions. Both the time-averaged velocity profiles (not shown) and the size and shape of the vortices are nearly identical suggesting that grid independence results have been obtained as long as a grid of 321 x 325 or better is employed. Therefore, all results discussed below employed this resolution.

Note that, although this resolution appears quite large, the unique advantage of the LBE method is that even with such a high resolution, a typical simulation (i.e., around 7-10 flow through times) can be completed overnight on a single processor SGI Power Challenge. This is to be contrasted to the computational time of several days when using a conventional finite-volume scheme. Therefore, in spite of the high grid resolution employed here, the LBE simulations are considered quite cost effective.

4.3 Flow field outside and inside the synthetic jet cavity

As observed in the experiments, when forcing is applied at the bottom of the cavity a periodic fluid motion occurs through the cavity orifice. In the absence of mean flow (as is the case here), the sinusoidal forcing generates no net mass flow into the domain but does introduce momentum into the fluid flow region. This is an unique feature of the synthetic jet when compared to conventional microjet blowing/suction method where both mass and momentum can be introduced. During the outflow portion of the forcing cycle as the fluid exits from the orifice due to the shear relative to the surrounding external flow a vortex ring is shed from the orifice lip. This vortex ring propagates downstream at a velocity close to the forcing amplitude U_o. Continuing the forcing results in a periodic shedding of these vortex rings at the forcing frequency, as shown in Fig. 5a. This flow feature is in excellent agreement with experimental observations. The shed vortices propagate downstream at a relatively constant phase velocity without significant decay. However, the coherence of the shed vortices far downstream is probably an artifact of the present 2D simulation since no external turbulence and/or 3D effects are included here. Experimental data suggests that as the shed vortices propagate away from the orifice they begin to diffuse and breakdown due to 3D turbulence and vortex stretching effects. Although this feature is not captured here, in the near field (were turbulence effects have not yet begun to effect the coherence of the shed vortices) the present results are in good agreement with experimental observations.

Figure 5b shows the instantaneous vorticity contours inside the synthetic jet cavity for Case 1. At $\omega t = \pi/3$, outflow is just beginning and the formation of primary vortices can be seen. At around $\omega t = 4\pi/3$, the shed vortex is moving away from the jet cavity orifice and the suction cycle is just beginning. During the suction period of the cycle, there is actually a vortex shedding process into the cavity at the lip of the orifice. However, due to the limited size of the cavity, the vortex structure impinges on the bottom wall (as in a impinging jet) and spreads along the bottom wall and up the side wall (as shown at $\omega t = 0$). A portion of this fluid shear layer on the walls of the cavity becomes part of the vortex that is shed from the orifice during the next cycle. Note that before the suction period begins the shed vortex ring has already moved out into the external fluid. As a result, the fluid sucked into the cavity does not come from the fluid in the vortex structures but rather from the wall boundary layers outside the cavity. This behavior is an experimentally observed feature of the synthetic jet actuator.

4.4 Parametric study

Figure 6 compares the predicted (normalized) velocity profiles at various axial locations with the experimental data of.[22] There is reasonable agreement with data in the central region of the jet flow indicating that self-similar evolution has been achieved. There is, however, some discrepancies at the outer edges of the jet shear layer. This is related to 3D nature of the vortex decay observed in the experiments and not modeled in the present 2D study, as noted earlier. Full 3D LBE studies (planned in the future) can be used to get better agreement in the outer layers and will be the subject of future studies.

Other cases were also studied as summarized in the table. Here, we discuss some of these results in order to determine if scaling laws can be developed. In cases 6-9 the cavity dimensions were systematically changed. Comparison with Case 1 shown earlier indicate some significant differences. As the orifice size is increased, the vortex shed during the injection period of the forcing cycle becomes smaller (not shown here for brevity but described in detail elsewhere[23]). This is probably related to the redistribution of the momentum through the orifice since the same momentum is being spread out over a larger area. This result suggests that to maintain coherence of the initial vortex ring the orifice size needs to be of a certain size for a given forcing frequency and amplitude.

Changing the cavity depth effects the flow dynamics both outside and inside the cavity. Again, comparison with Case 1 (the baseline case) is used to determine the impact on the vortex formation both inside and outside the cavity due to changes in the cavity depth. Decreasing the cavity depth does not appreciably affect the coherence and size of the vortices shed from the cavity. However, when the cavity depth is increased there is larger region of internal motion inside the cavity and some of the momentum inside the cavity is used to create a large vortex pair that propagates in a manner quite similar to the propagation seen outside the cavity. The shed vortex in this case does appear to be relatively weaker when compared to the other cases.

Thus, it is concluded that changing the jet cavity dimensions can have appreciable effect on the shed vortices and the net momentum transferred into the external flow. There appears to be a optimal configuration for a given forcing frequency (all studied noted above were for the same forcing frequency). Further study is planned to fully determine the relationship between the jet cavity shape and effectiveness of the actuator.

4.5 Mass and Momentum Flux Analysis

The mass and momentum flux through the orifice and at various axial locations was computed during the simulations to determine the effectiveness of the actuation process. Figure 7 shows the temporal variation of the mass flow rate through the orifice of the actuator for various forcing amplitude (Cases 3-5). The mass flux is normalized by the mass flux at the bottom wall of the cavity. Time average over the simulation period shows that the time-averaged mass flux through the orifice is zero even though there are some cycle-to-cycle variations. Figure 7 also shows that as the forcing amplitude increases the amount of mass moved through the orifice also increases. There is not much effect on the net mass flux when the orifice size is changed or when the cavity depth is changed (not shown here but given elsewhere[23]).

Analysis of the momentum flux through the orifice was also carried out. Figure 8a compares the momentum flux through the orifice and at an axial location $x/h = 36$. It can be seen that although the net momentum at the orifice exit plane is zero, the generation of the vortex causes an increase in net momentum further downstream. Figure 8b shows that there has been a net introduction of momentum into the flow by the synthetic jet with the momentum decreasing with axial distance. This decay in momentum with distance is likely to be underpredicted by the present 2D study. In 3D flows, the effective distance for momentum transfer to the bulk flow is likely to smaller due to vortex breakdown. Nevertheless, the present study demonstrates the unique feature of the synthetic jet to transfer momentum to the flow without adding mass.

Time-mean streamwise velocity at the same fixed streamwise location ($x/h = 11.8$) for different cases are shown in Figs. 9a,b. It is apparent that the average velocity at a fixed streamwise location will increase with the forcing amplitude. This is understandable since a larger amount of momentum is transferred with increase in forcing amplitude. However, the spreading of the jet is not significantly effected by increase in forcing amplitude. When the forcing frequency is changed, however, (Fig. 9b), both the peak centerline velocity and the spread of the jet is effected. Jets generated by a high frequency forcing are narrow but with a larger centerline velocity when compared to jets created by low frequency forcing. The increase in the mean velocity with increase in frequency is related to the fact that the jet gets more energy from a high frequency forcing over a given time period (for a fixed forcing amplitude).

The comparison of velocity profiles variations with different orifice size (not shown) show that the peak velocity decrease with increasing orifice size. That was also observed earlier in the vorticity structures and is related to the redistribution of the total momentum generated by the forcing over a larger area. However, interestingly, when the cavity depth is changed there appears to be no appreciable effect on the mean velocity profile.

The phase speed of the vortex ring moving away from the jet orifice for the various cases was computed using two-point correlations and summarized in Table 2. It can be seen that for a reference velocity of $U_o = 20m/s$, the phase velocity is around 16.2 m/s for Case 1 which is around $0.81U_o$. This is consistent with past observations. However, changing the forcing frequency, amplitude and cavity orifice size has a strong influence on the phase speed of the vortex ring. The effect of changing frequency is relatively benign, however, when the forcing amplitude is changed there is a large effect on the phase speed of the vortex ring. Making the cavity orifice size larger reduces the phase speed of the vortex ring drastically. Decreasing the cavity depth also decreases the phase speed.

These results suggest that in order to maintain a coherent synthetic jet from the orifice all these parameters need to be optimized carefully. The present study suggests some overall directions regarding this issues. Further study is still needed to fully understand the dynamics of the interaction between the flow inside and outside the cavity for various conditions.

4.6 Synthetic Jet actuated fuel injector

In this configuration, two options are evaluated: two synthetic jets placed inside the fuel jet with actuation normal to the primary fuel flow direction and two synthetic jets placed at the lip of the fuel injector with actuation parallel to the fuel flow direction. Figures 10a and b show respectively, these two configurations schematically. Both these configurations are being studied experimentally (using a more complex multiple synthetic jet configuration) and results have shown that although both orientations result in enhanced mixing, the axial forcing case is more effective. Although the present study is limited to 2D flows with only 2 synthetic jets, this issue can be addressed here.

The grid resolution for this case is increased so as to resolve both the synthetic jet cavity and the thickness of the fuel injector lip. The orifice size is still $h_o = 0.5mm$ and the fuel injector size is $3h$ with a lip thickness of $2h$ (Of course, these values can be changed in the future to represent a more realistic fuel injector, but the present study is focussed on demonstrating the feasibility of simulating a synthetic jet forced fuel injector). To evaluate interaction between two synthetic jets, the entire domain shown in the figure is simulated (i.e., centerline approximation is not invoked). A computational grid of 421 x 425 is used to resolve the computational domain with each of the cavity region resolved by more than 20x20 points. With this resolution, the out air flow stream diameter is not much larger than the fuel jet diameter. This is not a good approximation for a flow in the vicinity of a real fuel jet (where the surrounding air stream has a much larger extent). However, this is an issue that can be easily addressed later.

The two component LBE model is used with the fuel specie explicitly computed in the flow field. Spatial redistribution of the fuel specie in the domain outside the fuel injector is used as the key measure of the mixing efficiency of the synthetic jets. The effect of changing the forcing amplitude, frequency and phase of one jet relative to the other has been studied. Here, only representative results are discussed to demonstrate the ability of the synthetic jets.

Figure 11 shows a qualitative comparison of the instantaneous vorticity contours for different actuation strategies with the synthetic jets placed inside the fuel injector. Complex vortex shedding in the near field is observed. The vortices shed by the synthetic jet trigger an instability in the primary fuel stream (note that the primary fuel stream is not forced). As a result, the primary fuel stream undergoes unstable flapping motion and sheds vortices into the stream. The unforced jet also undergoes natural instability due to the flow around the nozzle lip; however, comparison with the other three cases show that the forced cases have more small-scale vortices and furthermore, the flow appears to have penetrated considerably into the air stream. Note that the scale of these vortices is quite small and is typically of the order of the fuel jet diameter or smaller. It can be seen that even if one injector is turned off significant instability in the fuel jet is created by the synthetic jet actuation. These vortical structures will play a major role in mixing.

The axial forcing also shows a similar flow field. Figure 12 shows an instantaneous comparison of the vorticity for the cases with and without synthetic jets. Both the normal and axial forced fuel jets are compared. Clearly, both types of forcing result in shedding of vortical structures similar in size. There are, however, some subtle differences that impact mixing. For example, the axial forced jet vortices appear to be less coherent and quickly diffuses in the air stream. Some of the implications are discussed below.

To make quantitative comparison, Figure 13a and 13b show respectively, the scalar profiles at two axial location for the different actuation strategies when the synthetic jets are inside the fuel injector. It can be seen that forcing increases the mixing in all the cases with the case of both jets ON (and in phase) showing the best results. When the amplitude of forcing is increased, mixing efficiency also increases as shown in Figure 14a. This increase in mixing is related to the generation of more coherent (i.e., stronger) vortices in the near field.

As observed in experiments, the axial forcing by the synthetic jets is much more effective in enhancing mixing. This is shown in Figure 14b where both axial and normal forcing is compared to the baseline unforced case. The species profile is spread out much more for the axially forced case. This is understandable since this configuration directly excites an instability at the interface between the fuel and coaxial air. As a result, vortices form by entraining both fuel and oxidizer as in classical shear layer except that the present structures are relatively smaller than the large-scale structures seen in forced shear layers. As these vortices diffuse out mixing is enhanced. In contrast, in the case with the synthetic jets inside the fuel jet the vortices are formed primarily in the fuel stream and mixing is enhanced only when these vortices penetrate into the air stream and undergo diffusion.

Which configuration is more practical for gas turbine combustor applications remains to be determined; however, note that when the synthetic jet is inside the fuel injector it is shielded from the hot combustion zone and therefore, may be more practical.

5 Conclusions

In this study, the Lattice Boltzmann method is being employed to simulate the flow field generated by synthetic jets. Results show that the LBE method is capable of simulating the unsteady flow field generated by the synthetic jet and further, the predicted results show reasonable agreement with experimental data. Since the current effort is limited to 2D flows, some discrepancies are seen in the far field in that the vortices generated by the synthetic jet persist for a longer distance than in real 3D turbulent flow. However, in the near field, the results are quite acceptable.

The present study also demonstrated the computational efficiency of the present LBE method. Even when very fine grids were used, the LBE calculation was orders of magnitude faster when compared to conventional finite-volume approach. This computational efficiency of the LBE code is essential for the next phase of development which will involve full 3D.

Finally, the synthetic jet model was implemented within a typical fuel injector to determine the impact of synthetic jet forcing on the mixing of fuel and air. As shown above, results show that synthetic jet actuation can increase the mixing efficiency of fuel injector. Axial forcing was found to be more efficient in agreement with experimental observations. There are many parameters that can effect the mixing efficiency of the synthetic jets: the effect of phase between the two jets, frequencies of the forcing, forcing amplitude and even the primary fuel flow rate. Parametric studies of these effects are underway and will be reported soon.

Acknowledgments

This work was supported by the Army Research Office under a grant DAAG55-98-1-0495 and monitored by Dr. David Mann.

References

[1] Glezer, A. and Allen, M., "Vectoring and small scale motions effect in free shear flows using synthetic jets," *AFOSR Contractors Meeting*, 1996.

[2] Ho, C.-M. and Tai, Y.-C., "Review: MEMS and its applications for flow control," *J. Fluid Engg.*, Vol. 118, 1996.

[3] Tseng, F.-G., Linder, C., Kim, C.-J., and Ho, C.-M., "Control of mixing and micro injectors for combustion applications," *ASME DSC*, Vol. 59, 1996.

[4] Rizzetta, D. P., Visbal, M., and Stanek, M., "Numerical Investigation of Synthetic Jet Flowfields," *AIAA 98-2910*, 1998.

[5] Kral, L., Donovan, J. F., B., A., and Cary, A. W., "Numerical Investigation of Synthetic Jet Flowfields," *AIAA*, 1997.

[6] Beskok, A., Karniadakis, G., and Trimmer, W., "Rarefaction and compressibility effects in gas microflows," *J. Fluid Engg.*, Vol. 118, 1996.

[7] Piekos, E. S. and Breuer, K. S., "Numerical modeling of micromechanical devices using direct simulation Monte Carlo method," *J. Fluid Engg.*, Vol. 118, 1996.

[8] Oh, C. K., Oran, E., and Cybyk, B. Z., "Microchannel flows computed with DSMC-MLG," *AIAA Paper No. 95-2090*, 1995.

[9] Chen, H., Chen, S., and Matthaeus, W. H., "Recovery of the Navier-Stokes equations using a lattice Boltzmann method," *Phys. Rev. A*, Vol. 45, 1991.

[10] Chen, S., Wang, J., Doolen, G., and Shan, X., "Lattice Boltzmann computational fluid dynamics in three dimensions," *J. Stat. Phys.*, Vol. 68, 1992.

[11] Chen, S. and Doolen, G., "Lattice methods and their applications to reacting systems," *Annu. Rev. Fluid Mech*, 1998.

[12] Qian, Y. H., d'Humières, D., and Lallemand, P., "Lattice BGK models for the Navier-Stokes equation," *Europhys. Lett.*, Vol. 17, 1992.

[13] Qian, Y. H. and Orszag, S. A., "Lattice BGK models for Navier-Stokes equations," *Europhys. Lett*, Vol. 21, 1993.

[14] Nobel, N. R., Chen, S., Georgiadis, J. G., and Buckuis, R., "A rigorous hydrodynamic boundary condition for the lattice Boltzmann method," *Phys. Fluids*, Vol. 7, 1995.

[15] Hou, Q. Z., Chen, S., Doolen, G. D., and Cogley, A. C., "Simulation of cavity flow by the lattice Boltzmann method," *J.Stat. Phys*, Vol. 81, 1995.

[16] Alexander, F., Chen, H., Chen, S., and Doolen, G., "A lattice Boltzmann model for compressible fluid flows," *Phys. Rev. A.*, Vol. 46, 1992.

[17] He, X. and Luo, L.-S., "A priori derivation of the lattice Boltzmann equation," *Phys. Rev. E*, Vol. 55, 1997.

[18] Shan, X., "Simulation of Rayleigh-Benard convection using a lattice Boltzmann method," *Phys. Rev. E*, Vol. 55, 1997.

[19] Shan, X. and Chen, H., "Lattice Boltzmann model for simulating flows with multiple phases and components," *Phys. Rev. E*, Vol. 47, 1993.

[20] He, X., Luo, L., and Dembo, M., "Some Progress in Lattice Boltzmann Method: Part I. Nonuniform Mesh Grids," *J. Comput. Phys*, Vol. 129, 1996.

[21] He, X. and Luo, L.-S., "Lattice Boltzmann method on curvilinear coordinates system: flow around a circular cylinder," *J. Comput. Phys*, Vol. 134, 1997.

[22] Smith, B. L. and Glezer, A., "Vectoring and Small-scale Motions Effected in Free Shear Flows Using Synthetic Jet Actuators," *AIAA Paper No. 97-0213*, 1997.

[23] Menon, S., "Lattice Boltzmann Simulations of Fuel-Air Mixing excited by MEMS-based Synthetic Jets," *Computatational Cumbustion Lab., CCL-TR-001, Georgia Tech*, Vol. 1, 1999.

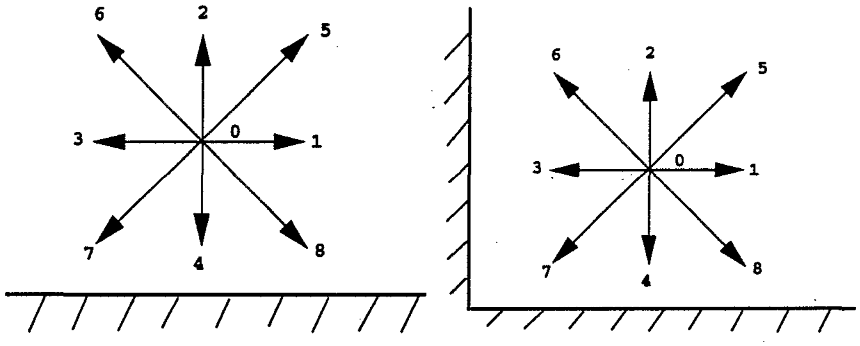

a) Velocity directions above a no-slip wall b) Velocity directions near concave wall

Fig. 1 LBE 9-bit velocity directions

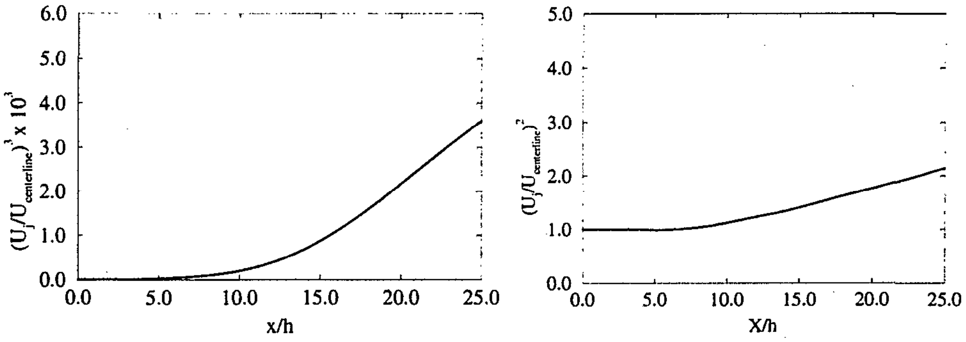

a) Laminar jet ($Re = 30$) b) Turbulent jet ($Re = 9000$)

Fig. 2 Centerline velocity decay. Here, U_j is the velocity at the jet exit and h is the orifice width. Results show that the jet achieves self similar decay for $x/h > 15$.

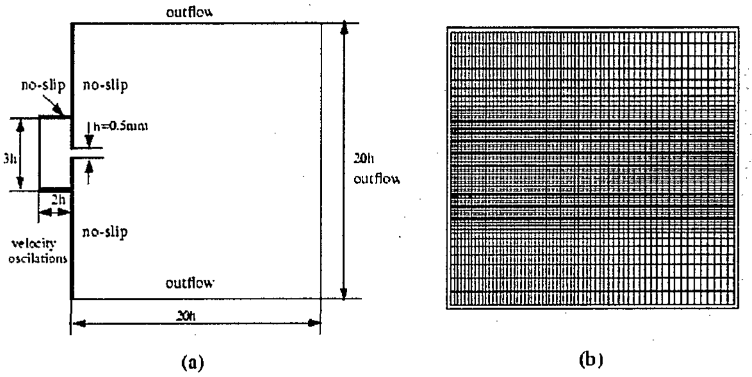

Fig. 3 (a) Computational domain and (b) Typical grid resolution

case1	case2 $f = 0.5f_0$	case3 $f = 2f_0$	case4 $U = 0.5U_0$	case5 $U = 2U_0$	case6 $h = 0.75h_0$	case7 $h = 2h_0$	case8 $d = 0.5d_0$	case9 $d = 2d_0$
16.2	15.02	21	3.8	25	22.4	5.76	8.114	18.3

Table 2 Phase speed for different cases.

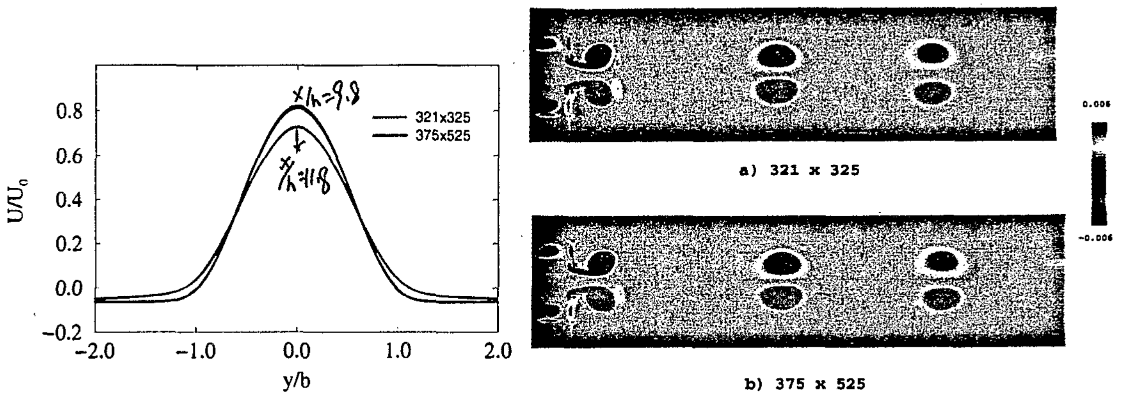

a) Mean streamwise velocity profiles b) Vorticity contours

Fig. 4 Grid independence study

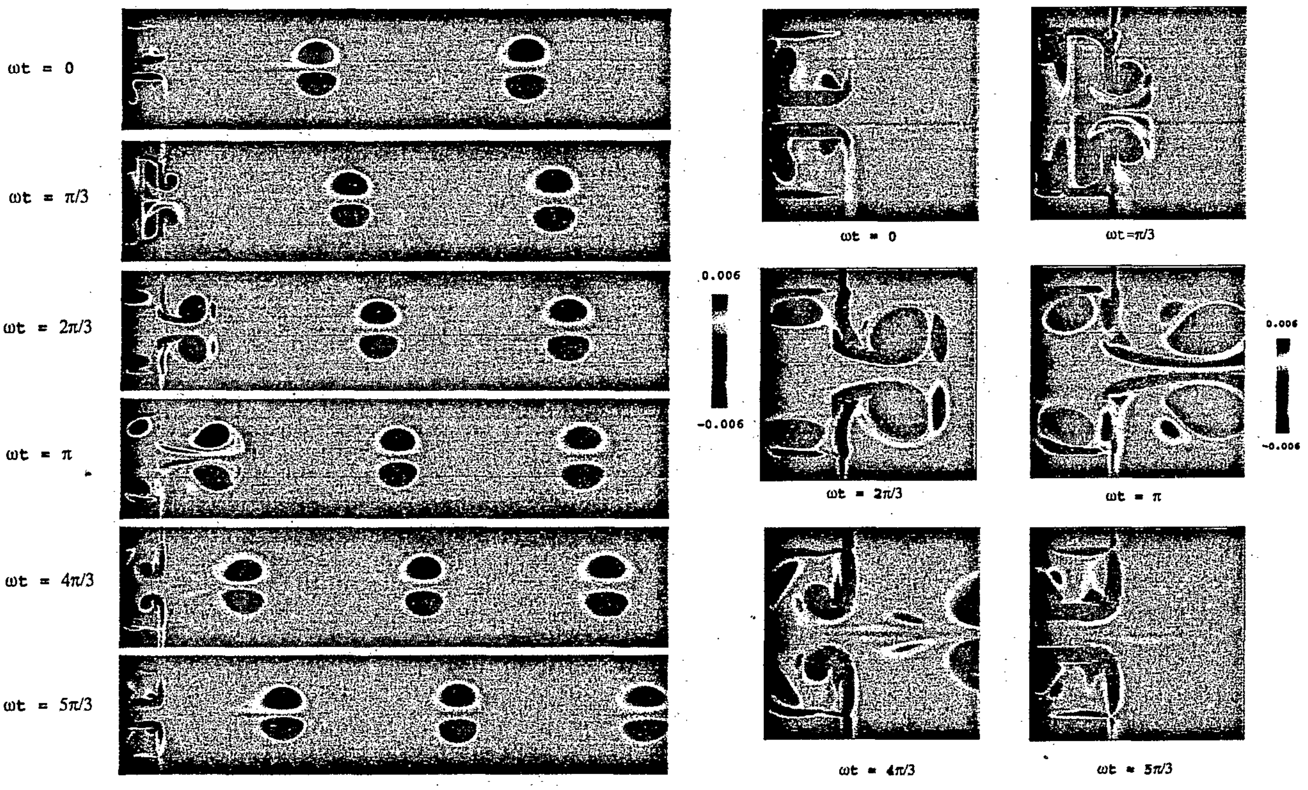

a) Outside the jet b) Inside the cavity

Fig. 5 Vorticity contours during a forcing cycle for Case 1

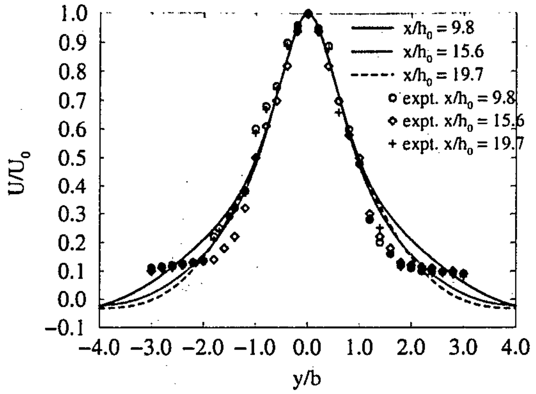

Fig. 6 Comparison of the normalized velocity profiles at various axial locations with experimental data from Smith and Glezer, 1997

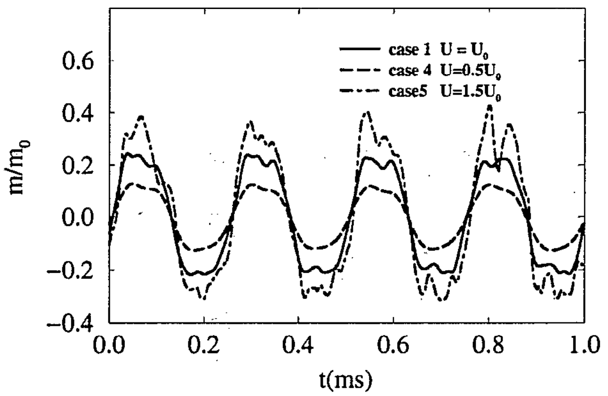

Fig. 7 Mass flux through the orifice for various forcing amplitudes.

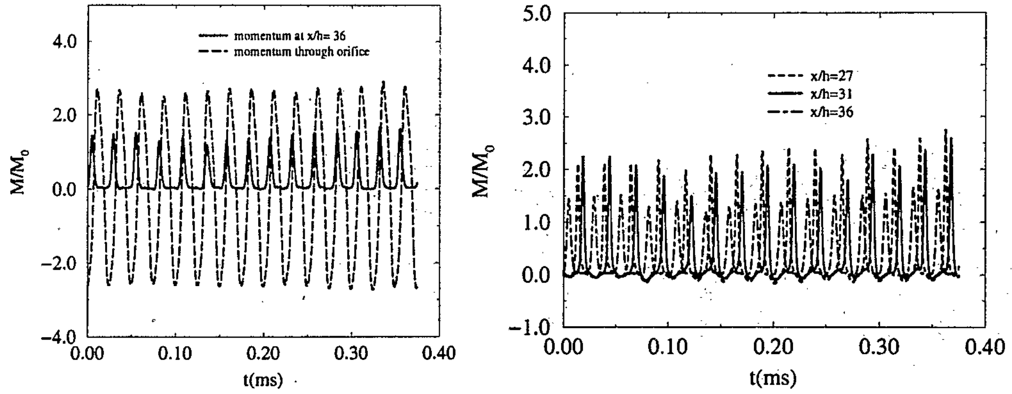

a) At $x/h = 0, 36$

b) At various x/h

Fig. 8 Momentum flux balance outside the synthetic jet. A net positive momentum is imparted into the fluid by the actuation.

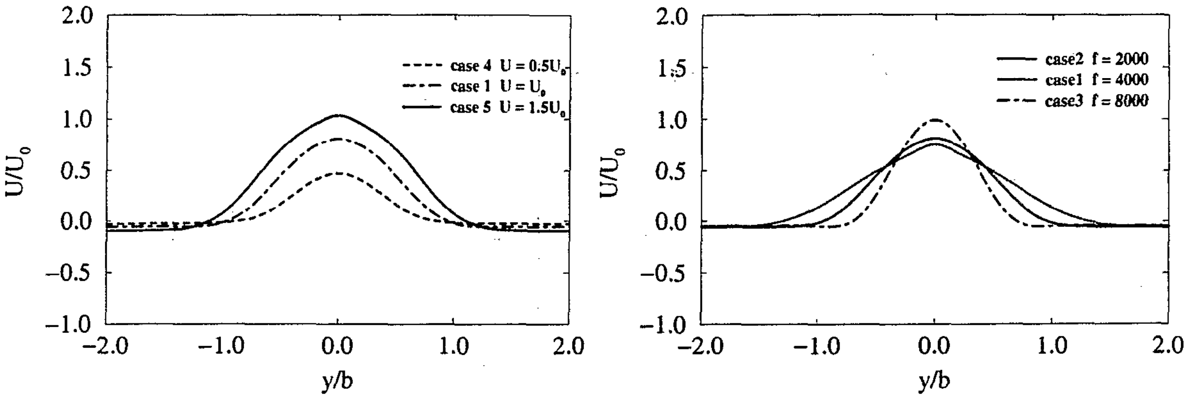

a) At different amplitudes b) At different frequencies

Fig. 9 Mean velocity profiles at $x/h = 11.8$.

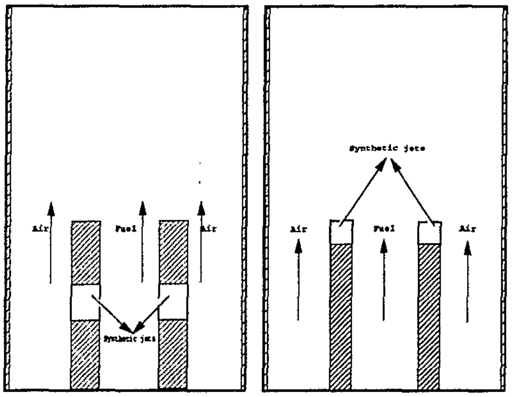

a) Normal excitation b) Axial excitation

Fig. 10 Computational domain fuel injectors with embedded synthetic jets.

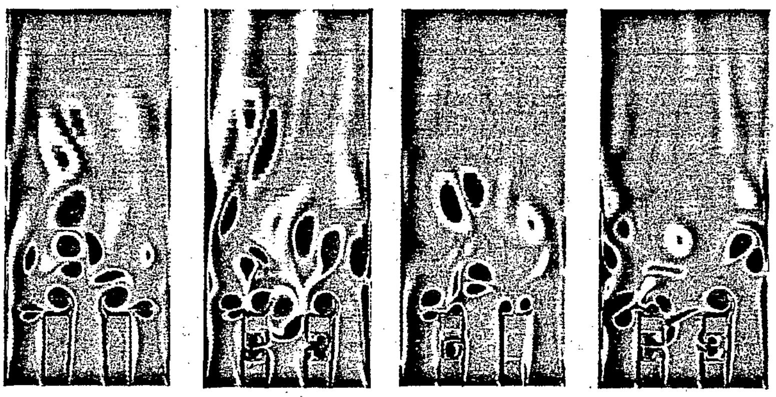

a) No forcing b) Both jets ON c) One jet ON d) Both jet ON at 90 phase

Fig. 11 Instantaneous vorticity contours for normal forcing.

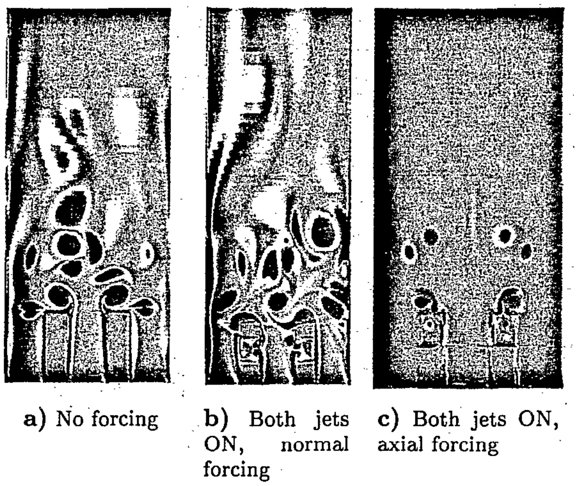

a) No forcing b) Both jets ON, normal forcing c) Both jets ON, axial forcing

Fig. 12 Comparison of vorticity contours for normal and axial forcing.

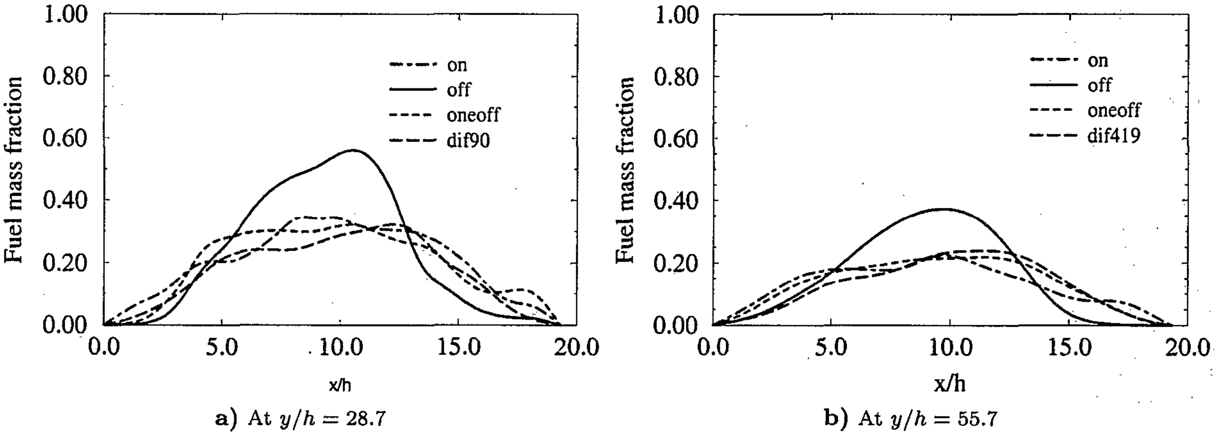

a) At $y/h = 28.7$ b) At $y/h = 55.7$

Fig. 13 Fuel mass fraction profiles for normal forcing conditions.

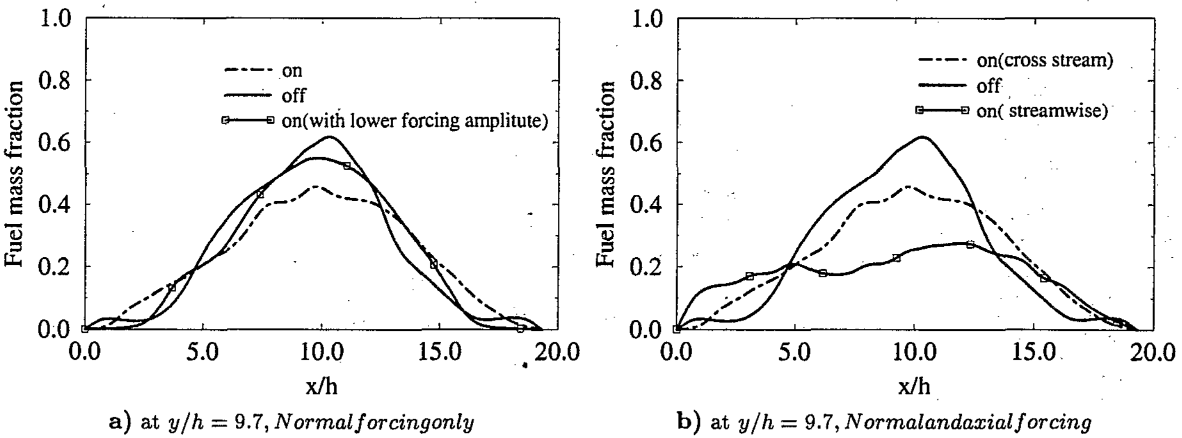

a) at $y/h = 9.7, Normal forcing only$ b) at $y/h = 9.7, Normal and axial forcing$

Fig. 14 Fuel mass fraction profiles for different forcing conditions.